Research article

JGS
Journal of the Geological Society

https://doi.org/10.1144/jgs2025-161 | Vol. 183 | 2026 | jgs2025-161

# Debritic head formation during the Tōhoku-oki 2011 tsunami reveals enhanced risk in mud-rich coastlines

**Patrick D. Sharrocks[1]*, Jeffrey Peakall[1], Natasha L. M. Barlow[1,2], David M. Hodgson[1], James McKay[1] and Hajime Naruse[3]**

[1] School of Earth and Environment, University of Leeds, LS2 9JT, Leeds, UK
[2] Haskoning, 1 Aire Street, Leeds LS1 4PR, UK
[3] Kyoto University, Kyoto, Japan
PDS, 0009-0000-5810-0635; JP, 0000-0003-3382-4578; NLMB, 0000-0002-2713-2543; DMH, 0000-0003-3711-635X; HN, 0000-0003-3863-3404
* Correspondence: eepsha@leeds.ac.uk

**Abstract:** Tsunamis pose a major hazard, exaggerated by large floating debris within the flow. However, understanding of how finer sediment (sand, silt and clay) influences the tsunami flow remains incomplete, introducing uncertainty in predictive models of their impact. Typically, a turbulent and dilute tsunami wave is assumed, but the differing conditions at the flow front have yet to be quantified. Here, videos of the 2011 Tōhoku-oki tsunami in the Sendai Plain, Japan, were analysed to document trends in the properties of the tsunami flow front. Results reveal rapid temporal and abrupt spatial changes in velocity and the development of a steep gradient to the flow front (~25–59°). Deposits reveal the tsunami flow had a high mud content and caused almost continuous erosion for at least 2 km inland. This evidence shows that a highly cohesive flow with a dense debritic head formed in the mid-shore region, transforming from an initially turbulent flow through the entrainment of cohesive material. The altered hydrodynamics and the greater force exerted by a dense debritic head highlight the need to incorporate debritic heads into tsunami hazard assessments on mud-rich coastlines, where the hazard will be enhanced.

**Supplementary material:** Supplementary figures that detail the processes undertaken to determine the flow front velocities and flow front gradients at the study sites are available at https://doi.org/10.6084/m9.figshare.c.8376881

**Received** 8 August 2025; **revised** 17 March 2026; **accepted** 17 March 2026

Tsunamis are large waves generated by earthquakes, volcanic eruptions, submarine and/or subaerial landslides, and impact events. The recent devastating 2004 Indian Ocean and 2011 Tōhoku-oki tsunamis have driven enhancements in mitigation strategies (Strusińska-Correia 2017) and improved predictions of future events through probabilistic tsunami hazard assessments (PTHAs) for vulnerable coastlines (Løvholt *et al*. 2014; Behrens *et al*. 2021). Since these events, it has been common to describe tsunamis as 'debris-like flows' because of the prevalence of wood fragments, plastics and even cars being moved in the flow (Borrero 2005; Fritz *et al*. 2006; Synolakis and Kong 2006). This debris adds an extra dimension to the tsunami damage and risk, with an added loading effect on buildings, people and structures impacted by the flow (Nistor *et al*. 2017; Kaida *et al*. 2024). This effect is now widely considered in structural design and in estimating damage from future tsunami events (Nistor *et al*. 2017; FEMA 2019), although the effect of debris is not considered in hydrodynamic modelling (Behrens *et al*. 2021). In contrast, the lack of direct measurements of the flow means that the sediment type and concentration of tsunamis are largely unknown (Goto *et al*. 2014; Mitra *et al*. 2020), limiting our understanding of the flow rheology and density. Therefore, we currently cannot determine whether this larger debris is carried by a tsunami flow that is fully turbulent and dilute or laminar and highly cohesive (Mulder and Alexander 2001; Baas *et al*. 2009), flow states that have vastly different hazard implications (Thouret *et al*. 2020). Herein, we address this problem by evaluating the fluidal flow properties of the Tōhoku-oki 2011 tsunami through application of a novel methodology to video footage of the event.

The flow state (turbulent to laminar) of environmental flows is governed by the flow Reynolds number (*Re*), defined as the product of the flow speed and flow depth over the kinematic viscosity of the flow. Higher Reynolds numbers are associated with turbulent, dilute flows and lower values with laminar, cohesive flow states (i.e. debris flows). Therefore, given the high velocities and depths of tsunami flows (Goto *et al*. 2011), they are typically assumed to be highly turbulent and dilute flows in sedimentological (Moore *et al*. 2011; Takashimizu *et al*. 2012) and experimental studies (Yoshii *et al*. 2018), although the flow viscosity is rarely considered (Yamashita *et al*. 2025). However, other environmental flows can transform between these states rapidly in time and abruptly in space (Fisher 1983), often through entrainment of large quantities of sediment, particularly cohesive muds, by an initially turbulent flow (Peakall *et al*. 2020). This increased sediment concentration increases the cohesivity of the flow, progressively dampening turbulence and moving the flow towards, or in cases to, a laminar flow state (Baas *et al*. 2009; Peakall *et al*. 2020). Although tsunamis erode and entrain copious volumes of sediment (Richmond *et al*. 2012; Takashimizu *et al*. 2012), such flow transitions have yet to be considered as tsunamis are assumed to reach only modest sediment concentrations of up to 2–7% by volume (Goto *et al*. 2014; FEMA 2019).

Many aspects of tsunami sediment transport are well known. Tsunamis are widely acknowledged to erode and entrain large quantities of sediment from the immediate coastal zone (on- and offshore), depositing this sediment as the wave slows further inland (Morton *et al*. 2007; MacInnes *et al*. 2009). This transport and deposition are suspension dominated, as demonstrated by sedimentary analysis of modern and ancient events (Morton *et al*. 2007; Szczuciński *et al*. 2012), experimental studies (Yoshii *et al*. 2018) and numerical modelling (Jaffe *et al*. 2016). This suspended load in the tsunami flow increases the sediment concentration of the

tsunami flow, with estimates varying from 2% from *in situ* data from the 2011 tsunami (Goto *et al.* 2014) to 5% for some experimental studies (Yoshii *et al.* 2017, 2018), with guidelines of 5–7% in building design regulations (FEMA 2019). At such modest concentrations, the high-velocity tsunami flow could be described as a turbulent, relatively dilute flow, and the behaviour of the flow can be assumed not to be affected by the suspended sediment (Pierson 2005). As such, numerical models of tsunamis that underpin PTHAs assume constant viscosity and densities equivalent to seawater (Marras and Mandli 2020). However, these concentration estimations are averages that fail to capture any internal variability within the flow.

The internal variations in flow dynamics and sediment transport within tsunami flows are less well understood. Observations or measurements inside the tsunami flow are virtually impossible due to their rarity and high magnitude. Furthermore, sediment transport models that aim to simulate past events are constrained by an incomplete understanding of sediment transport during tsunamis (Jaffe *et al.* 2016), despite recent improvements (Mitra *et al.* 2020). In particular, these models cannot account for any internal density stratification in the flow either vertically, with a denser basal component (Jaffe *et al.* 2016; Sugawara 2021), or horizontally, with a higher concentration flow front, where sediment entrainment is concentrated in tsunamis (Apotsos *et al.* 2011). Such spatial changes in flow concentration have recently been proposed for tsunami events in Scotland (Hill *et al.* 2023) and the Andaman Islands (Majumdar and Bhattacharya 2025), where sedimentary evidence indicated deposition under a basal or frontal cell with sediment concentrations in excess of 20–30%. In addition, Sharrocks *et al.* (2025) used sedimentary observations from tsunami deposits in coastal lakes to interpret rapid flow transformations and increases in flow concentrations. In such examples, a high-concentration, cohesive flow state would be predicted at the base or front of the flow, whilst the rest of the flow remains relatively dilute (<5% sediment concentration). This longitudinal separation of a denser head or base and dilute flow body is well described in other environmental flows such as subaqueous gravity currents (Haughton *et al.* 2009; Peakall *et al.* 2020; Baas *et al.* 2021). Whilst these flows may be used as an analogue for how such states may develop, the scale, extent and processes for their development in tsunamis, if present, are unknown as denser flow states have not been considered in observations of the flow front, and numerical models are unable to resolve such fine-scale processes.

Observations of modern events can provide more information on the motion, characteristics and evolution of the flow front of the tsunami as it inundates the land. The advent of mobile phone cameras and rapid rolling news coverage in the last few decades has meant that recent tsunamis have been captured (Fritz *et al.* 2006; Sihombing *et al.* 2019; Borrero *et al.* 2023), allowing for an analysis of the hydrodynamics of tsunami waves. In the nearshore, these observations have commonly shown tsunami waves forming spilling breakers (Röbke and Vött 2017), which induce turbulence and create a highly turbulent wave shortly after landfall (Morton *et al.* 2007). However, further inland studies of the flow rheology are limited to estimations of the flow velocity (Fritz *et al.* 2006; Goto *et al.* 2011) and depth (Fritz *et al.* 2006; Sato *et al.* 2014) and are widely used in the validation of numerical models (Hayashi and Koshimura 2013; Jaffe *et al.* 2016). These measurements have allowed a representation of some aspects of the flow dynamics of modern events, but video observations have not been employed to determine finer scale flow dynamics at the flow front, such as spatial and temporal heterogeneity in the velocity, height and steepness that can allow a greater understanding of the flow type (high concentration and cohesive, or dilute and turbulent).

Here, we use video footage of the 2011 Tōhoku-oki tsunami in the Sendai Plain to analyse the spatial and temporal variations in flow properties (velocity, depth and gradient) at the flow front. These flow parameters are coupled with sedimentary data and more extensive video footage of the tsunami to examine the evolution of the flow-front behaviour across the Sendai Plain. We integrate these results to provide a model of tsunami flow-front evolution over the study area. The model demonstrates that the tsunami transformed from a turbulent to a high-concentration state and formed a cohesive debritic head in the mid-shore region due to the erosion and entrainment of cohesive mud into the flow. This provides an opportunity to re-evaluate risk assessments on mud-rich coastlines where tsunamis have the potential to form debritic heads.

## Study area

The Tōhoku-oki tsunami of 11 March 2011 was generated by an Mw 9.0 earthquake on the Japan Trench boundary, 130 km off the NE coast of Japan (Simons *et al.* 2011). This tsunami affected 2000 km of coastline and resulted in 19 000 fatalities (Mori *et al.* 2011). Here we focus on the area of the Sendai Plain (Fig. 1) where flows showed the greatest inland inundation of 5 km (Mori *et al.* 2011) and where helicopter-based video coverage of the tsunami wave was captured (Fig. 1). On this plain, land use before the tsunami predominantly consisted of rice paddy fields with several semi-urban areas (Fig. 1c). The coastline is backed by a narrow beach (100–150 m wide) with an elevated coastal dune located landward that was planted with Japanese black pines during the last 400 years to protect rice paddies from salt incursion or as a response to the 1611 Sanriku tsunami (Tappin *et al.* 2012) (Fig. 1b). The Teizan canal transverses the landscape between 500 and 1000 m inland, beyond which lay less extensive dune deposits (Fig. 1b). The rest of the study area up to the inundation limit consists of back marsh or abandoned channel deposits of sand and clay (Matsumoto 1985; Ozawa *et al.* 1987). In the years before the tsunami, numerous hard and soft engineering structures had been installed on this coastline as a defence against coastal erosion and as protection from tsunami waves (Tappin *et al.* 2012). These may have affected propagation of the tsunami in the nearshore. Numerous sedimentary transects were conducted across the Sendai Plain 2 months after the event to examine the deposits produced by the tsunami (Goto *et al.* 2011; Abe *et al.* 2012). This included one transect north of Sendai Airport (Fig. 1b) where extensive sedimentary (Szczuciński *et al.* 2012), geochemical (Chagué-Goff *et al.* 2011) and microfossil (Pilarczyk *et al.* 2012) data were collected. These data can provide valuable information on the sedimentary composition of the wave over time.

## Methods

### Flow-front velocity

The NHK World helicopter video (resolution: 1280 × 720, frame rate: 29.97 Hz), available via CNN's YouTube (NHK World 2011), captured the tsunami wave moving over the Sendai Plain over 18 min and 13 s (NHK World 2011). This video has been previously analysed to calculate average flow velocities (Hayashi and Koshimura 2013), although only at a single point on the flow front, and thus the authors were not able to assess the degree of spatial variation in the front velocities. Here, we re-analyse this footage, which provides the widest view available of the tsunami flow front, to assess the spatial and temporal variations in flow properties (velocity, depth and gradient) of the tsunami flow front. However, video stills are not presented due to the sensitive nature of the images, and paintings were used instead. A reprocessed, higher-resolution version of the footage (resolution: 3559 × 2002, frame rate: 30 Hz) was used where possible, with the coverage lasting from 17:10 to 19:10 min (NHK World 2011, 2021; available via NHK

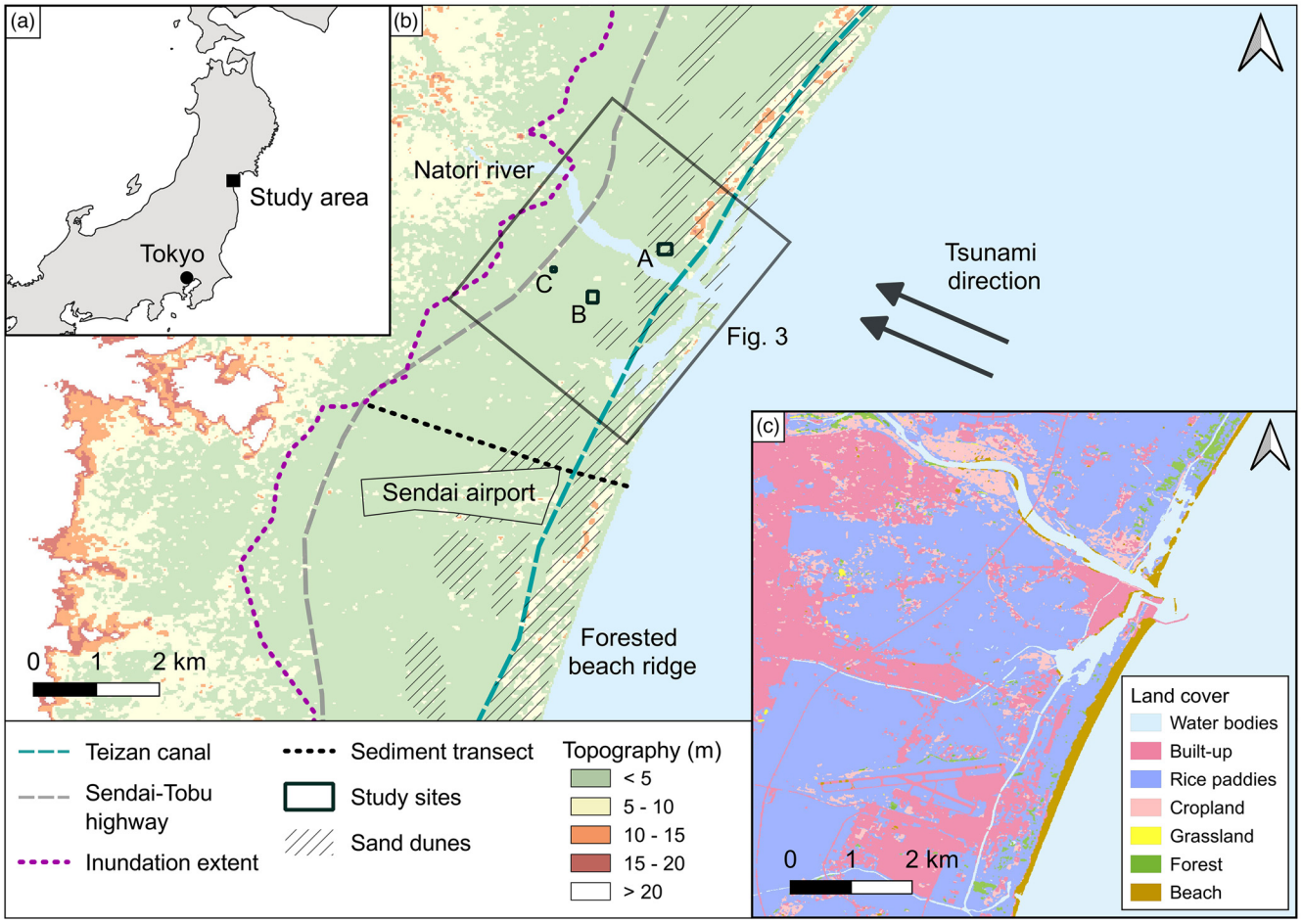


**Fig. 1.** Map showing site locations and key features of the study area. (**a**) Location of the study site within Japan. (**b**) Topographic map of the Sendai Plain study area; key features are identified including the inundation extent of the Tōhoku-oki 2011 tsunami and the location of a transect where sediment deposits were collected. Areas where dune deposits comprise the surface geology are shown. (**c**) Pre-tsunami land cover (2006–11) map covering approximately the same area as (b). Source: the data used in this figure were provided through Earth Explorer SRTM 1 Arc-Second Global dataset; ALOS of the Japan Aerospace Exploration Agency (Ozawa *et al*. 1987; Mori *et al*. 2011).

World); this corresponded to two periods from 0 to 0:55 and from 3:15 to 4:00 min in the original footage. The two videos are referred to as videos X (NHK World 2011) and Y (NHK World 2021) respectively. Periods during the video were selected based on where the flow progressed over a relatively stable field of view for at least 20 s to allow the temporal variations in the tsunami velocity and flow front morphology to be assessed. These video sections were then correlated to specific locations using freely available historical satellite aerial imagery acquired through Google Earth Pro for 4 April 2010 and 14 August 2009. The two locations were site A to the north and site B to the south of the Natori River, approximately 1 and 1.9 km inland respectively (Fig. 1b). Both locations were covered by the higher resolution video Y, providing a clearer image from which to track the flow front, minimizing the uncertainty in our measurements. Other sections of the video were deemed of insufficient resolution for accurate assessment of the flow velocity, although a third site, C, at the inland limit of the video was considered in more detail in our qualitative analysis of the flow variations.

At each location, the field of view remained similar for 20 s, and this allowed video Y to be divided into five individual frames (Supplementary Fig. 1a) at 5 s intervals corresponding to 18:11, 18:16, 18:21, 18:26 and 18:31 min through the video at site A, and 18:50, 18:55, 19:00, 19:05 and 19:10 min at site B. The visual markers that were present in each frame, such as field boundaries, polytunnels and stationary buildings, were then correlated to the same features in historical imagery (Supplementary Fig. 1a, b). This provided a reference location for the frame. The wavefront was then traced onto the historical aerial imagery in Google Earth Pro using these visual markers across the length of the frame (Supplementary Fig. 1c). This process was repeated for each 5 s interval at both sites, which provided a time series of the tsunami wavefront (Supplementary Fig. 2). This methodology was chosen over other techniques such as object detection and tracking within the flow (Foytong *et al*. 2013), as these techniques only estimate the velocity of the flow body rather than the flow front. An evolving velocity field was then visualized using an interpolation workflow. First, the wavefronts were projected into the UTM coordinate reference system to allow linear distances to be measured. Then along every wavefront, 100 equally spaced points were plotted, and lines were created to connect these points on each successive pair of adjacent wavefronts. The length of each line was assigned as the distance travelled over the timestep between two wavefronts. This timestep was defined as the difference in time between wavefront pairs, i.e. 5 s. Using the time and distance travelled, the velocity between each pair of points was calculated (400 velocity points per site) and the value interpolated to the midpoint of each of the connecting lines between two wavefronts. Interpolation was conducted using ShaPy (Pollard *et al*. 2024), an algorithm designed to interpolate between two margins, in this case, two wavefronts. The resulting velocity field was visualized in a Plate Carree projection using the Cartopy library so patterns in the data could be seen. This was repeated for sites A and B. The velocity calculated at the extremes of the observed wavefront was anomalously large compared to elsewhere

(>14 m $s^{-1}$) due to edge effects caused by the differing lengths of the wavefronts that could be plotted from the videos. Similar large velocities were also recorded at the extremes of site B; these velocities at the edges were not used in any subsequent analysis.

### Flow-front gradient

The height and gradient of the tsunami flow front were estimated using videos X and Y. The tsunami front is shown to pass through and over objects such as vehicles, buildings and polytunnels. The polytunnels were common across much of the agriculture-dominated plain, and relatively high-resolution video footage showed the tsunami wave impacting polytunnels at site A. These polytunnels were identified on pre-tsunami imagery from 14 August 2010, and higher quality imagery from 1 September 2008, which were used to measure the dimensions of the polytunnels in Google Earth Pro (Supplementary Fig. 3a). Multiple measurements were taken across the width ($n = 5$) and length ($n = 7$) of the larger polytunnels at site A and average values calculated to provide the width and length of each polytunnel. The length of the smaller, adjacent polytunnels to the north was also measured ($n = 23$). The precision of these measurements was taken to be decimetre scale due to the uncertainty in measuring distances from satellite imagery. The polytunnel height could not be measured using historical imagery as 3D imagery or Street View were not available before the tsunami. Therefore, modern polytunnels of similar morphology in the study area were identified and their height was measured using Google Earth 3D view from the present day (Supplementary Fig. 3b). The height of each polytunnel in a row of 11 was measured and an average was taken. The height of the flow front was then calculated based on the height relative to the known polytunnel dimensions.

To measure the length of the flow front, the flow direction first had to be determined in each image. This was achieved using historical 2009 satellite imagery in a QGIS environment to trace the flow front for each of the six selected video frames for the previous 2 s of the flow. A flow direction was then drawn between the point on the later flow front where the gradient will be measured and the nearest point on the earlier wavefront. To transfer this flow direction to the video images, the angle between the flow direction and the axis of the polytunnels was measured in QGIS. A flow direction could then be accurately drawn on to the video image at the same angle to the polytunnel axis (direction arrow in Supplementary Fig. 4). The length of the flow front was then measured in a parallel direction to this calculated flow direction to ensure the gradient was calculated parallel to the flow front. To measure the length of the flow front, two points were taken, one at the flow front and a second at the first point where the flow front could be observed to be as high as the maximum height of the polytunnel (i.e. at the midpoint of the polytunnel). From this second point, a line perpendicular to the flow front was drawn (shown in yellow in Supplementary Fig. 4). Finally, a line parallel to the flow front direction was drawn from the first point until the intersection with the previous line, and this was taken as the length of the flow front. This length was measured using ImageJ software with a scale set to the length of either the larger or smaller polytunnels depending on which polytunnel type was utilized in each image. The measured length and height of the flow front were then used to calculate the angle of the flow front, equal to the gradient (Supplementary Fig. 5):

$$\text{Gradient} = \tan^{-1}(\text{length}/\text{height}) \quad (1)$$

This was repeated for six different video frames at site A (video times of 18:14, 18:15, 18:19, 18:20, 18:21 and 18:24; see Supplementary Fig. 4). Due to the uncertainties in the gradient measurement, a specific value for the flow-front gradient was not assumed and instead a range of values were given. One cause of the uncertainty was the distortion in the video images due to their oblique angle (Verykokou and Ioannidis 2024), with the top right of the video frames at site A appearing as longer distances than reality due to the camera position. However, the effects of distortion were reduced as the scale used and flow-front length measurements were taken in the same portion of the image.

Other stationary objects (e.g. vehicles and buildings) that the tsunami flow front was observed to have passed through or over also show the flow-front height and gradient. However, height measurements were difficult from the video footage due to the generally low resolution outside of the study sites, which added to the uncertainty in estimating the height of buildings that did not survive the impact of the tsunami. In limited locations, heights were estimated for building features including windows and porch heights through which the flow front was observed to flow. The flow-front width and gradient were measured using the same methodology as for the polytunnels, but the building features were used instead of the polytunnel height (Supplementary Fig. 6). Where the flow-front width could not be measured, only a height was estimated.

## Results

### Video analysis of flow-front properties

The spatial–temporal variation in the flow front is visualized in Figure 2. The statistical values given were derived from the 400 velocity measurements calculated at each site between each pair of wavefronts, with the highest and lowest 5% of velocities excluded as outliers. At site A, the velocity ranged from 2.9 to 13.1 m $s^{-1}$ with a median velocity of 7.1 m $s^{-1}$. This is consistent with the velocity measurements made by Hayashi and Koshimura (2013), who used a single point on the flow front through time, measuring a velocity of 7–7.2 m $s^{-1}$ across the same area. Here, we show the spatial variation in the velocity, with some sections of the wavefront varying by at least 8 m $s^{-1}$ over the 20 s period, with most areas of the flow front showing a change in velocity of at least 4 m $s^{-1}$ over this period (Fig. 2a). This reflects a pulsing behaviour to the flow front.

At site B, velocity was typically lower with values mostly between 2 and 10 m $s^{-1}$ and a median velocity of 4.1 m $s^{-1}$ (Fig. 2b). The velocity was also highly variable with a velocity change of up to 8 m $s^{-1}$ over the 20 s period (Fig. 2b), although in some areas of the flow front, the variability was lower (Fig. 2b). These velocities are comparable to the 3.4 m $s^{-1}$ measured by Hayashi and Koshimura (2013) at site B. The velocity values calculated at both sites also lie within the values measured for tsunami flow fronts at other urban sites on the Japanese coastline inundated by the 2011 tsunami, with velocities varying between 2.92 and 9.56 m $s^{-1}$ (Ngo and Robertson 2012). Overall, our measurements are consistent with prior research but also highlight marked spatial changes in wavefront morphology, indicating strong spatial–temporal variations in velocity across the flow front (Fig. 2).

The degree of variation in the velocity at sites A and B showed the flow front was moving non-uniformly with a pulsing behaviour. This provides insight into the flow type of the tsunami front. In dilute turbulent flows, such as rivers and turbidity currents, variation in the velocity is confined primarily to vertical rather than horizontal changes within the flow front, resulting in a relatively uniform flow-front velocity (Shige-eda and Akiyama 2003). In unconfined turbulent flows, such as overwash storm surges, spatial variability in the flow-front velocity is evident due to acceleration or deceleration around or over natural topographic features in a landscape, such as sand dunes (Warner *et al.* 2025). However, elevation models (Fig. 1b) and the video footage show that the landscape the tsunami front at sites A and B passed over was essentially flat, with few obstacles to the flow front that can alter the flow velocity (Farizan *et al.* 2019).

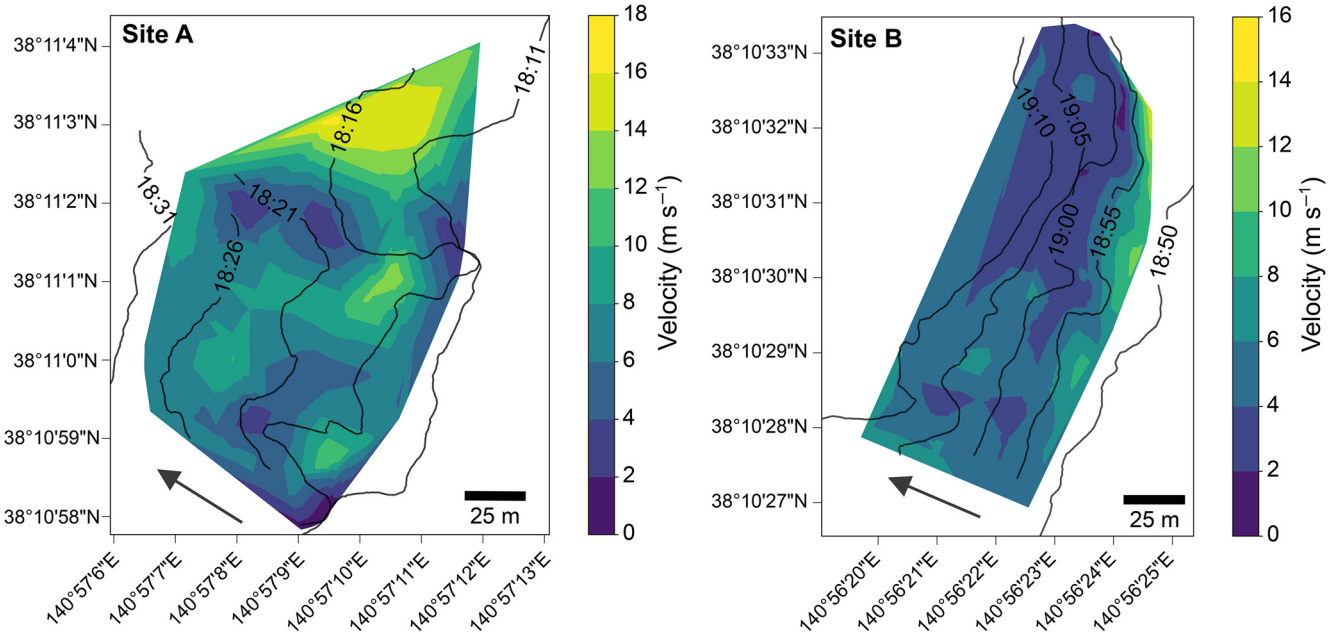


**Fig. 2.** Spatial velocity plots for the Tōhoku-oki tsunami front at the study sites. The velocity of the tsunami wavefront plotted on a spatial–temporal scale between 18:11 and 18:31 min of the tsunami video Y footage at site A and between 18:50 and 19:10 min of the footage at site B. The black lines represent 5 s intervals of the wavefront with the approximate wave direction shown by arrows. The top right of both plots shows areas of anomalously high velocities, which were due to the edge effects caused by the differing lengths of wavefronts that were recorded (see Methods). Note that the pronounced colour changes observed in the planform map represent rapid spatial and temporal changes in flow-front velocity, indicative of a pulsing flow.

Furthermore, temporal changes in storm surges over coastal plains can be rapid due to the short wave period (10–25 s), unlike the 2011 tsunami, which consisted of waves 10–20 min apart. Flow deceleration also occurs over time across flat ground due to friction, but cannot explain the magnitude of the spatial–temporal variability over the ~250 m that the two study sites cover. Therefore, the strong spatial–temporal variations in velocity at sites A and B (Fig. 2) would be difficult to explain if the flow front was highly turbulent and dilute, especially at site B where few obstacles are present.

In contrast, debris flows, whose highly cohesive fluidal phase comprises water mixed with sand, silt and clay, are unsteady and move in a non-uniform manner (Iverson 1997). They are characterized by a pulsing flow behaviour commonly cited as developing through the formation of roll waves (Zanuttigh and Lamberti 2007) that form at lower Froude numbers (>0.74) in laminar flows (Wang *et al*. 2021), or due to the formation of erosion–deposition waves (Schöffl *et al*. 2023). In high-concentration debritic flows, surges can originate from small variations in the sedimentary composition of the flow, which can act to amplify initial disturbances (Zanuttigh and Lamberti 2007; Kunath *et al*. 2025). With each initiation mechanism, the surges cause a local acceleration in the flow front as the head becomes denser and faster under continuous erosion during the flow (Breien *et al*. 2008). However, between surges, the flow front can come nearly to a halt with subsequent surges remobilizing or merging with the previous surge of the flow (Schöffl *et al*. 2023). This results in a fluctuating flow-front velocity profile during the flow, with peak flow velocity up to three times higher than average values (Zanuttigh and Lamberti 2007). The tsunami front velocities exhibit a similarly fluctuating profile (Fig. 2) that resembles the surging behaviour of debris flows. A similar surging behaviour was also observed in video footage of a viscous debris-laden tsunami flow from the 2004 tsunami in Banda Aceh at locations a similar distance inland (1.5–3 km) (Chanson 2006). However, this surging behaviour is not picked up in numerical models of tsunamis (Marras and Mandli 2020). Overall, the velocity evidence suggests the flow front was debritic at the two sites (1 and 1.9 km inland).

To provide further evidence as to the flow type of the tsunami, the flow-front gradient was estimated where the tsunami front engulfed polytunnels at site A (Supplementary Fig. 4). Engulfing of similar polytunnels was also observed a few hundred metres further inland in video X (1:08–1:12 min). This indicated the height of the flow front was at least as tall as the polytunnel height, measured to average 3.2 m (SD = 0.04 m) (Supplementary Fig. 3). To measure the gradient of the flow front, a length scale was established using the dimensions of the polytunnels. At site A, the larger type of polytunnels had an average width of 3.8 m (SD = 0.01 m) and length of 34.4 m (SD = 0.5 m) (Supplementary Fig. 3), whereas the smaller polytunnels had an average length of 13.5 m (SD = 0.09 m). These dimensions were used to measure the length of the flow front (up to the height of the polytunnels), as between 6.9 and 1.9 m across the six video frames (Supplementary Fig. 4). From this the gradient of the flow front was calculated to range between 24.9 and 59.3° (average = 35.9°; SD = 14.8°). Overall, the gradient values suggest that the tsunami front was very steep, albeit with large variability in estimated gradients.

In addition, the gradient of the flow front could be estimated where the flow travelled through the outside porch of a house (Supplementary Fig. 6). This has an estimated height of 2 m, a flow-front length measured at 13.7 m, giving a gradient of 8.3°. At Sendai Airport, video footage showed the flow front level with luggage carriers with an estimated height of 0.5–1 m, although a flow-front length and gradient could not be estimated. Overall, the gradient estimations provide a range of values between 8.3 and 59.3° with a flow-front height of at least 0.5–3.2 m.

The height and gradient of a flow front are useful indicators of the flow type due to the differences in gradients of turbulent and debritic flow fronts. For a dilute turbulent flow, the flow front typically has a shallow gradient due to the lack of cohesive forces that can hold the flow together (Talling *et al*. 2012). A steep flow front can develop in specialized cases such as tidal or tsunami bores (e.g. Tappin *et al*. 2012) and dam-break floods (Chanson 2006). Tsunami bores were only observed during the Tōhoku-oki tsunami in the immediate coastal zone (Tappin *et al*. 2012), with no bore evident in the videos

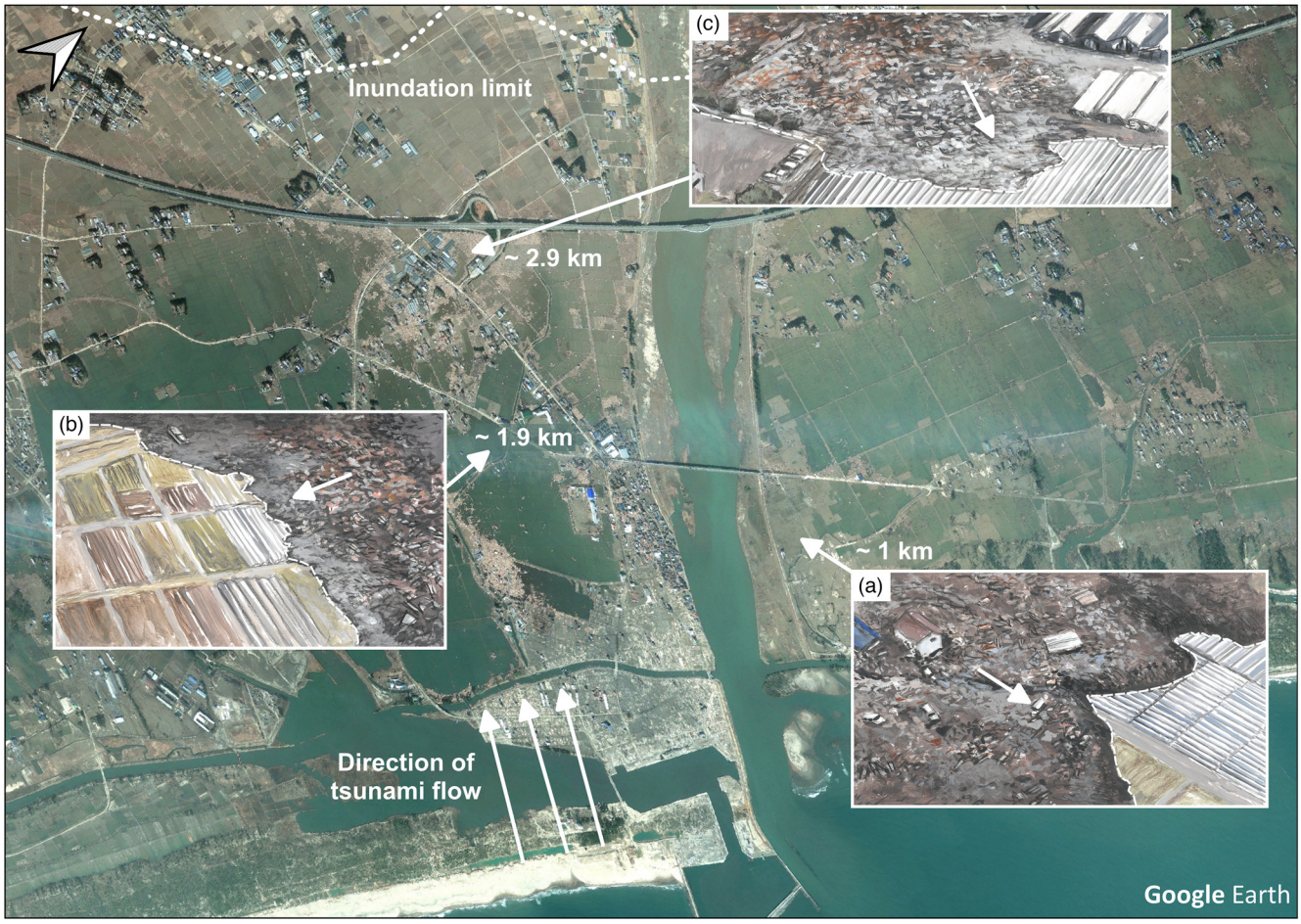


**Fig. 3.** Area covered by the tsunami video footage and variations in the tsunami front appearance between the study sites. (**a**) Painting of the video at site A (18:26 min (NHK World 2021)); (**b**) painting of the video at site B (18:55 min (NHK World 2021)); (**c**) painting of the video at site C at the inland limit of the coverage (11:40 min (NHK World 2011)). Background map shows post-Tōhoku-oki tsunami Google Earth imagery (14 March 2011) in the area covered by the NHK helicopter video; the area between site C and the inundation limit (white dashed line) was not covered during video footage. Arrows on each image indicate the direction of flow. The approximate distance inland is indicated for each video frame. Note that paintings are used, since NHK no longer license the reproduction of images, although the videos are available online and are linked to here (NHK World 2011, 2021).

at the two study sites >1 km inland (NHK World 2021). The locations of the study sites herein also preclude the formation of steep flow fronts through waves breaking at the shoreline (Sugawara *et al.* 2014). Dam-break flows can provide a useful analogy to tsunami flow during initial inundation or after overtopping a coastal barrier (e.g. Syamsidik *et al.* 2019; von Häfen *et al.* 2022). However, the study sites are neither on the immediate coastal zone nor situated proximal to a large topographic barrier. Therefore, the position of the study sites >1 km inland suggests these specialized conditions could not form and a steep flow front cannot be explained by a dilute turbulent flow. In contrast, the higher sediment concentration (of up to 30–50% by volume (Iverson 1997)), cohesion and density of a debritic flow front enables the flow to reach its maximum depths near to the flow front (Iverson 1997). This results in generally steep flow fronts (McCoy *et al.* 2010). Therefore, the very steep tsunami flow front measured at site A of between 24.9 and 59.3° indicates the flow type was debritic rather than turbulent. Overall, the video analysis showed that the flow front exhibited a pulsing behaviour with variable velocities and a very steep gradient, which are characteristics consistent with a debritic flow type at the study sites.

## Flow variations across the Sendai Plain

The flow velocity and height data provide a perspective of the flow front at two sections of the tsunami flow where conditions were similar. A more continuous narrative is provided by observations from videos X and Y of the flow over longer temporal and spatial scales as shown in Figure 3. In the nearshore, the wave appeared initially turbulent (Sato *et al.* 2014, their figure 2), especially as it passed through the forest of the coastal plain (Fig. 1b). As the wave progressed inland, the flow surface was observed to become gradually smoother in appearance, suggesting dampened turbulence (Fig. 3a). This part of the tsunami flow, covering sites A and B, was also visually darker and more viscous than in the nearshore and carried large amounts of debris, including vehicles and fragments from destroyed buildings, within the flow (Fig. 3a, b). Here, the pulsing, viscous flow front more closely resembles that of highly cohesive mudflows including volcanic lahars (Thouret *et al.* 2020) than a dilute clear water flood. A similar flow condition was observed a few kilometres inland during the 2004 tsunami in Banda Aceh (Chanson 2006). Further inland (towards site B), the flow carried a greater quantity of and larger debris, with fires evident amongst the debris carried by the flow over flat agricultural fields (Fig. 3b), suggesting a significant solid component (clays, silts) to the fluid. Further observations from nearby Sendai Airport (~1–1.5 km inland; Fig. 1b) depict a similarly dark, viscous and debris-laden flow (Takashimizu *et al.* 2012). After site B, around 1.9 km inland, video X continued to follow the progress of the wavefront further inland. The camera focused on an area around 2.9 km inland, site C (Fig. 3c), where the tsunami front was visually similar to that of sites A and B with a viscous, debris-laden flow,

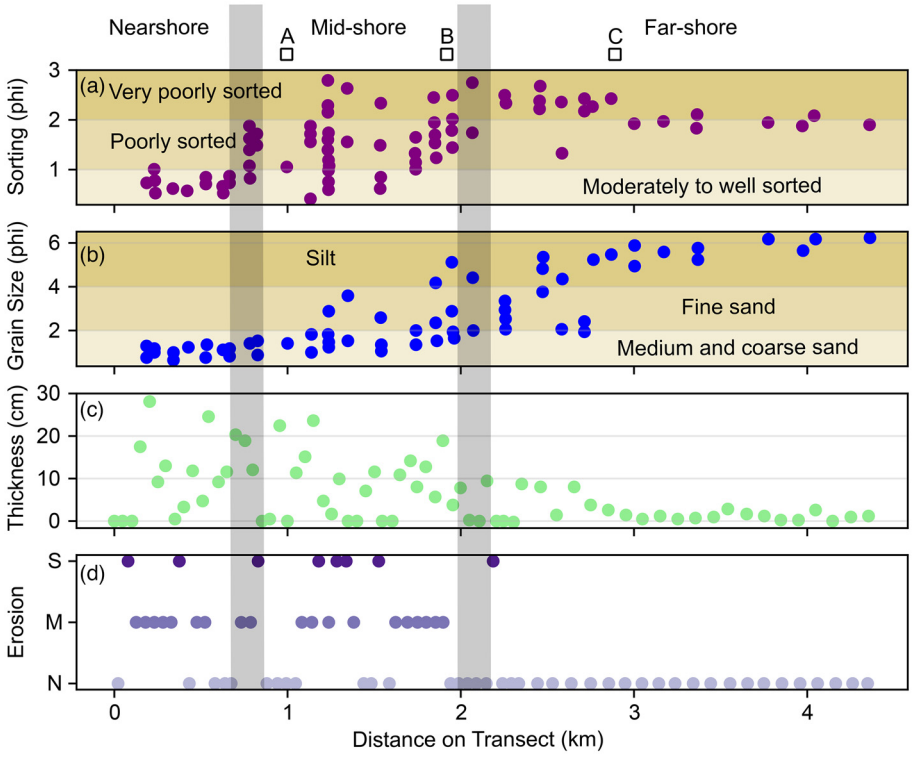


**Fig. 4.** Sedimentary data of the Tōhoku-oki tsunami from a transect taken immediately north of Sendai Airport. (**a**) Sorting of the tsunami deposit along the transect, categorized into very poorly, poorly, and moderately to well sorted. (**b**) Mean grain size of the deposits. (**c**) Average thickness of tsunami deposits over the transect. (**d**) Relative erosion along the transect (S = significant; M = moderate; N = little or no erosion). The approximate distance inland of the video study sites A, B and C are indicated above, along with the divisions of the near-, mid- and far-shore, which are shown by vertical shaded lines. Source: data replotted from Szczuciński *et al.* (2012).

albeit a flow that was visually far slower and carrying smaller and less abundant debris. The remaining approximately 1 km of inundation inland was not covered during the video, so the flow front could not be assessed. In summary, the observations from the video footage showed that over the Sendai Plain, the tsunami transformed from an initially highly turbulent state to a more debritic flow front further inland (Fig. 3).

## Sedimentary evidence

To determine the mechanisms behind the tsunami flow front transformation, the sedimentary evidence for the tsunami on the Sendai Plain was assessed. Tsunami deposits on the Sendai Plain varied with distance inland. The beach represented an area of erosion and no deposition, followed by deposits that were sand-dominated up to 2–2.5 km inland (Chagué-Goff *et al.* 2011; Goto *et al.* 2011; Abe *et al.* 2012; Richmond *et al.* 2012; Matsumoto *et al.* 2023) (Fig. 4b). From this point to the inundation limit, up to 4.85 km inland, the deposits were mud-dominated (Goto *et al.* 2011; Abe *et al.* 2012). This transition was generally smooth with an intermediary region between ~1.4 and 2–2.5 km inland where the grain size indicated a sandy mud or muddy sand deposit (Abe *et al.* 2012; Szczuciński *et al.* 2012) (Fig. 4b). In addition, deposits consisted of well- to moderately sorted sand in the nearshore up to ~750 m inland, before becoming poorly sorted sandy mud and finally very poorly sorted mud (Szczuciński *et al.* 2012) (Fig. 4a). Such a shift to more poorly sorted sediment generally reflects a flow increasing in sediment concentration that restricts sorting and segregation within the flow (Hiscott 1994). Moreover, erosion was shown to be strongest in the nearshore and decreased in prevalence inland with little or no evidence of erosion after ~2 km inland (Richmond *et al.* 2012; Szczuciński *et al.* 2012) (Fig. 4d). These erosional patterns were determined by the degree of erosional features identified during field surveys after the event (Richmond *et al.* 2012; Takashimizu *et al.* 2012). Finally, the deposit thickness decreased inland with the mud-dominated deposits predominantly thinner than the sandy layers nearer the shore (Abe *et al.* 2012; Szczuciński *et al.* 2012) (Fig. 4c). Overall, the sedimentary data show that erosion dominated in the nearshore region, resulting in an initially sand-rich flow that increased in mud content and sediment concentration further inland.

The provenance of sediment in tsunami deposits in the Sendai Plain can also aid reconstruction of the sediment content of the tsunami flow. Marine taxa were virtually absent from the diatom assemblage analysed in the tsunami sediments, which comprised predominantly freshwater–brackish species (Szczuciński *et al.* 2012). The minimal contribution of offshore components to the deposits in the Sendai Plain was confirmed by other proxies including an absence of shells (Richmond *et al.* 2012), and foraminiferal (Pilarczyk *et al.* 2012) and heavy mineral assemblages (Jagodziński *et al.* 2012). The last of these studies also found that sediments within 1.5 km of the shore were derived from beach and dune deposits, and local soils, whereas further inland sediments were derived from soil. This evidence is consistent with diatom and grain-size evidence that indicates the sediment source in the nearshore was beach and dune sand, in the mid-shore was local soil, dune sand and canal sediments, and in the far-shore was local soil (Szczuciński *et al.* 2012).

Observational, sedimentary and field survey (erosional) data show that over the Sendai Plain, the tsunami was initially a turbulent sand-rich flow that transformed inland into a more debritic mud-rich flow front. Similar flow transformations are commonly observed in subaqueous sediment gravity flows, where during a single event the flow can transition between different states ranging from fluidal and turbulent turbidity currents through higher concentration but still partially turbulent transitional flows (*sensu* Baas *et al.* 2009), to laminar debris flows (Talling *et al.* 2012; Peakall *et al.* 2020). The front of these subaqueous flows will preferentially erode and concentrate the most mobile sediment in a system (Baas *et al.* 2021), much like in tsunami events where erosion is concentrated at the flow front (Apotsos *et al.* 2011). Where this erosion below the flow front is sustained, as it was for 2 km during the tsunami in the Sendai Plain, cohesivity and density can increase to the extent that a dense flow head develops that is segregated from the trailing, more fluidal body of the flow. This transition occurs due to the incorporation of fine sediment (mud) within the flow (Baas *et al.* 2021). If erosion

continues, the head can transform into a fully cohesive debritic flow (Kane *et al.* 2017; Baas *et al.* 2021). However, this can generally only occur in mud-rich systems where erosion is continuous (a characteristic attribute of tsunami inundation (MacInnes *et al.* 2009; Sugawara *et al.* 2014)), otherwise a more transitional flow front may form instead (Peakall *et al.* 2020). A similar process of bulking-up through sediment entrainment by a flow has been proposed for the transition between dilute watery flows and high-concentration debris floods in subaerial settings (Pierson 2005). Overall, this suggests that in the mid-shore region, the sustained erosion of an increasingly mud-rich substrate caused the tsunami flow front to transform into a cohesive debritic head.

## Reynolds number

It is evident that a debritic flow state with dampened turbulence developed in the Sendai Plain. However, whether it reached a laminar flow state is not certain. This transition can be quantified using its Reynolds number. In a clear water flow, the Reynolds number at site A would equal the product of the velocity (7.1 m $s^{-1}$) and flow depth (3.2 m, as the maximum measured front depth), divided by the kinematic viscosity of water ($1 \times 10^{-6}$ kg $m^3$ $s^{-1}$). Therefore, the Reynolds number would be $\sim 2 \times 10^7$, well within a turbulent flow regime. Here, the elevated sediment concentration of the cohesive flow front increases the flow's apparent viscosity compared to a clear water condition. The viscosity cannot be measured directly from video analysis due to its low resolution, but can be inferred from known relationships between the sediment concentration of a fluid and its viscosity. The addition of cohesive clays (Castro *et al.* 2021; Shen *et al.* 2024) increases the viscosity of a flow far more than non-cohesive sand and silt. Thus, for the Sendai Plain, where a mixture of sands and cohesive muds (eroded from rice paddies; Fig. 4) are entrained by the flow, a typical soil profile is used to calculate the flow viscosity (Julien 2010; Zarch *et al.* 2022). Using this relationship (Julien 2010), a $10^4$-fold increase in viscosity would require a flow with 50% sediment concentration to reach a laminar state. Such concentrations are reserved for highly concentrated debris flows, such as lahars, where the flow's motion is driven by the solid component as these flows travel downhill (Iverson 1997; Thouret *et al.* 2020). This is not apparent for the tsunami flow in the Sendai Plain, where the gradient is low, and thus a flow driven by the solid component could not reach the high velocities that are measured. Instead, the flow behaviour is more consistent with a lower concentration debris flow (hyperconcentrated flow) that may be of the order of 30–40% (Iverson 1997). This equates to an apparent viscosity of ~1000 times that of clear water and a Reynolds number of $\sim 2 \times 10^4$; thus, the flow front probably remains turbulent at site A. Further inland, the tsunami velocity and depth decrease by at least an order of magnitude (Mori *et al.* 2011), whilst the flow retains a high sediment concentration (Fig. 5). Hence, the Reynolds number would decrease and approach a laminar state. Overall, the estimated Reynolds number shows that the cohesive flow front had dampened turbulence but remained turbulent for at least 2 km inland, possibly transitioning to a laminar state as the flow thinned and decelerated towards the inundation limit.

## Model of tsunami flow-front evolution in the Sendai Plain

The transitions in tsunami flow-front conditions can be visualized in Figure 5 by combining the interpretations of the data presented here. In the nearshore, the flow front was visually turbulent, and the sedimentary evidence suggested the flow content was mostly sand-derived, being too coarse to increase the cohesivity of the flow (Jagodziński *et al.* 2012; Szczuciński *et al.* 2012). However, the flow in the mid-shore region after ~750 m inland becomes visually denser and the sedimentary evidence shows a near-continuous erosion of muddy soil until 2.0 km inland (Richmond *et al.* 2012; Szczuciński *et al.* 2012) (Fig. 4). This produced a tsunami flow with an increased proportion of mud the further inland it flowed (Goto *et al.* 2011; Abe *et al.* 2012) (Fig. 5a). The higher mud content and continuous erosion would have gradually, albeit rapidly, increased the cohesivity of the flow front (Baas *et al.* 2021). The evidence from the flow-front velocity and gradient from sites A and B within this zone (1.0 and 1.9 km inland respectively) confirms the front was debritic, suggesting a complete transition to a fully cohesive, debritic head occurred in the mid-shore region (Fig. 5a). This represents the first postulation of, and evidence for, a modern tsunami wave behaving as a cohesive debris flow.

After the virtual cessation of erosion ~2 km inland (Richmond *et al.* 2012) (Fig. 4), little sediment would have been added to the flow. However, the tsunami flow continues to contain a high proportion of mud and its visual appearance at site C depicts the front as a high-density, low-velocity head 2.9 km inland or around

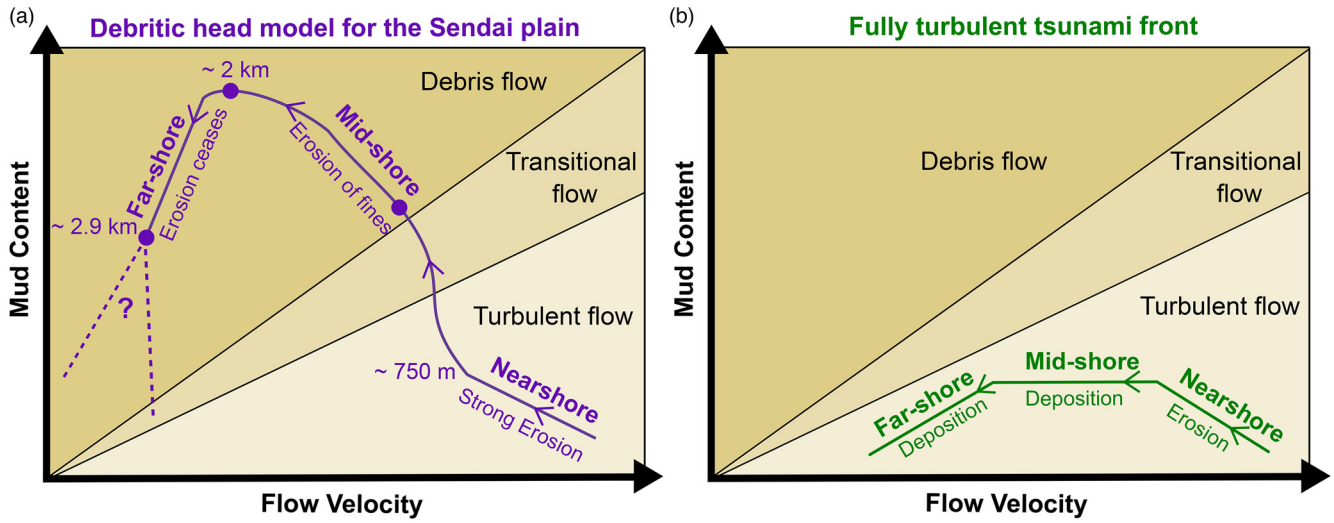


**Fig. 5.** Model of the tsunami flow-front evolution as a function of the flow velocity and mud content. (**a**) Tōhoku-oki tsunami flow-front evolution in the Sendai Plain with the distances referring to the approximate distance inland at different points on the schematic. The points on the line indicate the positions of the three study sites A, B and C. The dashed lines indicate the greater uncertainty close to the inundation limit. (**b**) The tsunami flow front if a fully turbulent flow was assumed throughout. Source: visualization based in part on Baas *et al.* (2021).

900 m from the inundation limit (Fig. 3c). This suggests that the head remains cohesive and debritic in character beyond the erosional limit (Fig. 5a). However, there is no direct information of the flow type beyond 2.9 km inland due to a lack of video or imagery of this section of the flow (Fig. 5a). Beyond ∼3 km the deposits are very thin (centimetric; Fig. 4), and consist of thin sands overlain by mud layers (Abe *et al*. 2012). This suggests that the debritic head probably stalled and was overtaken by the trailing, more fluidal flow, analogous to subaqueous hybrid flows where the debritic head is postulated to be overtaken by a low-concentration turbidity current as erosion ceases (Baas *et al*. 2021). This more fluidal flow is still mud-rich as shown by the deposits (Szczuciński *et al*. 2012) (Fig. 4), and undergoes sedimentation and thinning up to the inundation limit (Fig. 5).

Overall, the data show that the tsunami flow transformed inland from a turbulent, dilute flow front to a cohesive debritic head due to the entrainment of mud and deceleration of the flow. This is in marked contrast to widely held assumptions of a dilute and fully turbulent flow front throughout tsunami inundation (Moore *et al*. 2011; Yoshii *et al*. 2018; Marras and Mandli 2020), which would suggest little change in mud content and cohesivity further inland (Baas *et al*. 2021) (Fig. 5b). This standard dilute tsunami front model does not fit with the data presented for the Sendai Plain (Fig. 5).

## Discussion

Tsunami waves have been recognized to carry large, floating debris within the flow, but little was understood about the influence of the finer sediment (sand, silts and clays) on the flow, especially at the leading edge of the tsunami. However, using a novel methodology based on video analysis of the 2011 Tōhoku-oki tsunami, integrated with pre-existing deposit data (Goto *et al*. 2011; Abe *et al*. 2012), we have shown that the tsunami flow front transformed from an initially dilute turbulent state into a highly cohesive state, with a debritic head. This transformation was driven by sustained erosion and entrainment of mud-rich sediment and a concomitant increase in flow cohesivity. The evidence from the velocity, gradient and mud content of the flow front are all consistent with this dense debritic tsunami head having formed in the Sendai Plain. These findings contradict the current assumptions of a fully turbulent and dilute flow front commonly used within tsunami models, and hazard and risk assessments (Marras and Mandli 2020). Therefore, we need to reconsider how tsunamis are simulated and their risk in areas where a dense debritic head may form.

### Impact on tsunami models and hazard assessment

Current numerical models assume a clear water state and can accurately replicate the flow-front velocities in the Sendai Plain close to the coastline (Hayashi and Koshimura 2013). However, as the wave progresses inland, these models overestimate the flow velocity. In the case of the Sendai Plain, this is thought to be due to an incomplete parameterization of the frictional effects of floating debris on the flow (Hayashi and Koshimura 2013). However, the velocity measurements at sites A and B cannot match the model results from Hayashi and Koshimura (2013) even with changes to the frictional coefficient, which strongly influences flow velocity in models (Gibbons *et al*. 2022; Li *et al*. 2025). Instead, we suggest this discrepancy was due to the increased sediment concentration of the flow front, which influences the flow behaviour above concentrations of ∼4% (Pierson 2005). In high-concentration cohesive flows, as inferred at sites A and B, the vertical velocity profile differs from that of a clear water flow, with a laminar plug forming above turbulent conditions closer to the bed (Peakall *et al*. 2020). However, such internal flow stratification cannot be picked up within numerical models that do not resolve the internal physics of tsunami flows (Ortleb *et al*. 2022). Instead, the effect of enhanced sediment concentration can be simulated by using an elevated viscosity in numerical models. Taking a viscosity of ∼1000 times that of clear water for the Sendai Plain case analysed herein would dissipate the wave's energy as it progresses inland, lowering the flow velocity to more closely match the values measured here. However, enhanced viscosity has not been simulated for tsunamis (Marras and Mandli 2020) and should be the focus of future studies to quantify its effect on flow behaviour. Overall, there is considerable discrepancy between calculated flow velocities and numerical model simulations at the sites examined herein, probably caused by neglecting the effect of enhanced sediment concentration and flow viscosity in numerical models.

PTHAs are widely used to provide an estimation of the extent, magnitude and flow properties for a future event of a given probability (Grezio *et al*. 2017). However, they are generated using inverse and forward modelling techniques that assume a well-mixed low-density flow throughout inundation (Marras and Mandli 2020), a notion shown to be invalid for the Sendai Plain (Fig. 5). As seen at the study sites above, the elevated sediment concentration and viscosity of the flow front would alter the hydrodynamics of the flow (Mulder and Alexander 2001), resulting in differing values of the flow parameters, including flow density, velocity and depth, and the inundation distance, than those predicted by existing models (e.g. Hayashi and Koshimura 2013). Furthermore, within these models, it is difficult to accurately calculate the flow velocity at the wet and dry boundaries of the flow front, and thus the complex physics of the flow front is ignored (Ortleb *et al*. 2022). Therefore, the viscosity and density of the front itself cannot be simply altered in these models. This study highlights the need to develop a model (s) that can resolve the internal stratification in tsunami flows and to incorporate a sub-model into hazard assessments that considers the effect of elevated viscosity and density on the tsunami flow. The limitations in numerical models demonstrated by this study show that PTHAs may not accurately predict the tsunami hazard in the Sendai Plain (and in other similar areas). This has major implications for the many stakeholders who use PTHAs within the insurance, disaster-risk management and engineering sectors (Macabuag *et al*. 2018).

### Impact on tsunami risk assessments

The debritic nature of the tsunami in the Sendai Plain could have a major effect on the potential hazard of some tsunamis. In a given location, a high-concentration debris flow will generate more damage than a dilute and turbulent flow because the dense flow moving at high velocity exerts stronger pressures (Thouret *et al*. 2020). The destructive nature of overland dense debris flows is demonstrated by mudflows including lahars, which form on the slopes of volcanoes during eruptions where water mixes with sediment (Vallance and Iverson 2015). An example is the lahar generated by the Nevado del Ruiz eruption in Colombia where there were 23 000 fatalities and virtually all buildings were destroyed in its path (Lowe *et al*. 1986). Therefore, in the Sendai Plain, the formation of the dense debritic head during the tsunami inundation probably increased the damage associated with the event. A debritic tsunami flow front may also generate more damage than a turbulent, low-density flow front due to the greater force exerted by the denser debritic flow. Tsunami risk assessments use the flow parameters from PTHAs coupled with tsunami fragility and vulnerability curves to estimate the damage to infrastructure, the fatality rate and the injury rate for a given probability event (Dominey-Howes *et al*. 2010; Behrens *et al*. 2021). Due to a lack of direct data, these estimates are based on empirical models in which the most important estimator of damage is the hydrodynamic force of the

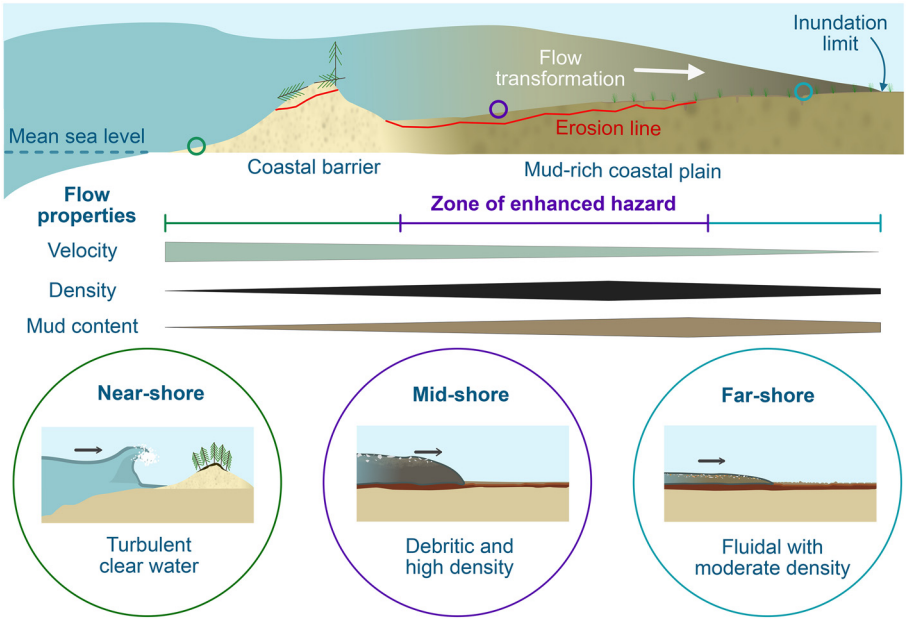


**Fig. 6.** Schematic model for the evolution of a tsunami over a muddy coastal plain. Cross-sectional view of a low-gradient, muddy coastal plain with the maximum inundation of the tsunami shown. Below are lateral trends in the flow-front properties (velocity, density and mud content) through inundation. Insets show the appearance and rheology of the flow front in the near-, mid- and far-shore, the last showing where the debritic head has been overtaken by a trailing, more fluidal flow.

flow (Macabuag *et al.* 2018). This is a function of the flow velocity and density, the latter being assumed to be the density of either water (Koshimura *et al.* 2009) (1000 kg $m^{-3}$) or seawater (Suppasri *et al.* 2015) (1025 kg $m^{-3}$). Building design guidelines by the Federal Emergency Management Agency (FEMA 2019) do, however, recommend that impact forces are calculated using a tsunami fluid density 1.1 times that of seawater (1128 kg $m^{-3}$). Nevertheless, such higher values are still rare within tsunami risk assessments (Behrens *et al.* 2021). A debritic flow front, as we have described in the Sendai Plain, would have a higher density still of between 1300 and 2200 kg $m^{-3}$(Thouret *et al.* 2020) leading to a higher hydrodynamic force on an object for a given flow velocity. This would generate greater damage to infrastructure, and potentially an increased fatality rate, than currently predicted in tsunami risk assessments. Furthermore, the second determinant of hydrodynamic force, velocity, is observed to show a fluctuating behaviour driven by surges in the flow front, making it difficult to accurately estimate the impact force at a given moment in time (Zanuttigh and Lamberti 2007; Kunath *et al.* 2025). Therefore, this suggests that where flow transformations take place during tsunamis, the current risk assessments are insufficient and should account for the combined effect of increased force and altered hydrodynamics in higher density flows. This inadequacy highlights the need to identify where such transformations take place.

## Debritic head formation beyond the Sendai Plain

This study has shown that flow transformations during a tsunami from a turbulent to high-concentration, cohesive state appear to be controlled by the ability of the flow front to continually erode and entrain cohesive sediment and the concomitant increase in mud content and flow cohesivity (Fig. 5a). The continual erosion and entrainment of sediment through inundation is a characteristic feature of large tsunami waves; thus, this criterion is commonly satisfied (Jagodziński *et al.* 2012; Szczuciński *et al.* 2012; Takashimizu *et al.* 2012; Sugawara *et al.* 2014). Instead, the major constraint on where flow transformations occur is the availability of cohesive mud-rich substrates and the ability of the tsunami wave to erode them. Therefore, flow transformations are likely to occur where readily erodible cohesive mud-rich substrates such as rice paddy fields, ponds and canals are found in the coastal zone. Such mud-rich coastal plains are found along parts of Sri Lanka, Indonesia and Thailand inundated during the 2004 Indian Ocean tsunami (Synolakis and Kong 2006), as well as other areas of Japan, such as the coastal areas of Chiba and Niigata prefectures (NCEI 2024). In these coastlines, the likely flow properties and rheology of a tsunami can be summarized as in Figure 6, using the analogy of the Sendai Plain. In contrast, on steep-gradient coastlines with sand-rich substrates, tsunami flows would entrain less cohesive mud and thus attain lower viscosities within a relatively dilute and turbulent flow front (Fig. 5b). Examples include some of the coastline of northern Chile impacted by the 2010 Chile tsunami (León *et al.* 2023) and on the northern Sanriku coast during the Tōhoku-oki 2011 tsunami (Ishimura and Miyauchi 2015; Abe *et al.* 2020). However, coastal plains are becoming increasingly mud-rich with the expansion of agriculture (Goldewijk *et al.* 2011) and land reclamation (Martín-Antón *et al.* 2020), especially in tsunami-prone regions of Japan where coastal grasslands and wetlands were converted to rice paddies during the twentieth century (Noda *et al.* 2019). This is depicted by the finer sediment content of the Tōhoku-oki 2011 tsunami compared to its predecessor, the Jogan 869 tsunami (Minoura and Nakaya 1991; Sawai *et al.* 2012). Therefore, future tsunamis may behave differently from their ancient analogues and be more likely to follow the scheme depicted in Figure 6 and develop a dense debritic front with the enhanced hazard this represents. Given these considerations, we suggest that land-use maps coupled with topographic data and widely available surficial geology maps that detail sand- and mud-rich substrates can be used to conduct a first-order assessment of the possibility of debritic head formation for a given location. This assessment would allow the identification of areas prone to debritic head development, and the potential enhanced hazard this represents, to be incorporated into tsunami risk assessments, improving forecasts of the impacts of future events. Furthermore, the novel methodological approach applied here could be used to determine the flow properties of future tsunami events through high-resolution videos.

We conclude that the Tōhoku-oki tsunami flow front in the Sendai Plain underwent rapid temporal and abrupt spatial flow transformation from a fully turbulent to a highly cohesive flow, and developed a debritic, high-density head. This transformation to a dense debritic flow was driven by the erosion and entrainment of a mud-rich substrate, which markedly increased flow cohesivity and viscosity (Fig. 5). This contradicts current assumptions of turbulent low-density flow fronts commonly used in tsunami risk assessments. The added force and altered hydrodynamics of a debritic flow front show that in mud-rich coastlines the tsunami risk will be

underestimated (Fig. 6). Therefore, identifying the limits of where a debritic tsunami flow front may form is vitally important to better inform coastal managers on the potential risk of future events.

*Scientific editing by Gene Rankey*

**Acknowledgements** We thank Professor Yuki Sawai for assistance with NHK discussions, and comments on an earlier version of the manuscript. We thank Professor Dave Mohrig, an anonymous reviewer and Editor Eugene Rankey for their constructive comments, which significantly improved the manuscript.

**Author contributions** **PDS**: conceptualization (equal), formal analysis (lead), investigation (lead), methodology (equal), visualization (lead), writing – original draft (lead), writing – review & editing (equal); **JP**: conceptualization (equal), funding acquisition (lead), methodology (equal), supervision (lead), writing – review & editing (lead); **NLMB**: conceptualization (equal), methodology (equal), supervision (supporting), writing – original draft (supporting), writing – review & editing (supporting); **DMH**: conceptualization (supporting), methodology (supporting), supervision (equal), writing – original draft (supporting), writing – review & editing (supporting); **JM**: visualization (equal), writing – original draft (supporting), writing – review & editing (supporting); **HN**: conceptualization (supporting), writing – original draft (supporting), writing – review & editing (supporting).

**Funding** This work was funded by the Natural Environment Research Council (NE/S007458/1).

**Competing interests** The authors declare that they have no known competing financial interests or personal relationships that could have appeared to influence the work reported in this paper.

**Data availability** All data generated or analysed during this study are included in this published article and its supplementary information files.

## References

Abe, T., Goto, K. and Sugawara, D. 2012. Relationship between the maximum extent of tsunami sand and the inundation limit of the 2011 Tohoku-oki tsunami on the Sendai Plain, Japan. *Sedimentary Geology*, **282**, 142–150, https://doi.org/10.1016/J.SEDGEO.2012.05.004

Abe, T., Goto, K. and Sugawara, D. 2020. Spatial distribution and sources of tsunami deposits in a narrow valley setting – insight from 2011 Tohoku-oki tsunami deposits in northeastern Japan. *Progress in Earth and Planetary Science*, **7**, 1–21, https://doi.org/10.1186/S40645-019-0318-6

Apotsos, A., Gelfenbaum, G. and Jaffe, B. 2011. Process-based modeling of tsunami inundation and sediment transport. *Journal of Geophysical Research: Earth Surface*, **116**, F01006, https://doi.org/10.1029/2010JF001797

Baas, J.H., Best, J.L., Peakall, J. and Wang, M. 2009. A phase diagram for turbulent, transitional, and laminar clay suspension flows. *Journal of Sedimentary Research*, **79**, 162–183, https://doi.org/10.2110/JSR.2009.025

Baas, J.H., Tracey, N.D. and Peakall, J. 2021. Sole marks reveal deep-marine depositional process and environment: implications for flow transformation and hybrid-event-bed models. *Journal of Sedimentary Research*, **91**, 986–1009, https://doi.org/10.2110/JSR.2020.104

Behrens, J., Løvholt, F. *et al.* 2021. Probabilistic tsunami hazard and risk analysis: a review of research gaps. *Frontiers in Earth Science*, **9**, 628772, https://doi.org/10.3389/FEART.2021.628772

Borrero, J.C. 2005. Field survey of northern Sumatra and Banda Aceh, Indonesia after the Tsunami and Earthquake of 26 December 2004. *Seismological Research Letters*, **76**, 312–320, https://doi.org/10.1785/GSSRL.76.3.312

Borrero, J.C., Cronin, S.J. *et al.* 2023. Tsunami runup and inundation in Tonga from the January 2022 eruption of Hunga Volcano. *Pure and Applied Geophysics*, **180**, 1–22, https://doi.org/10.1007/S00024-022-03215-5

Breien, H., De Blasio, F.V., Elverhøi, A. and Høeg, K. 2008. Erosion and morphology of a debris flow caused by a glacial lake outburst flood, Western Norway. *Landslides*, **5**, 271–280, https://doi.org/10.1007/S10346-008-0118-3

Castro, C., Borges, A.L.deO. and Manica, R. 2021. A new empirical viscosity model for composed suspensions used in experiments of sediment gravity flows. *RBRH*, **26**, e22, https://doi.org/10.1590/2318-0331.262120210048

Chagué-Goff, C., Schneider, J.L., Goff, J.R., Dominey-Howes, D. and Strotz, L. 2011. Expanding the proxy toolkit to help identify past events – lessons from the 2004 Indian Ocean Tsunami and the 2009 South Pacific Tsunami. *Earth-Science Reviews*, **107**, 107–122, https://doi.org/10.1016/J.EARSCIREV.2011.03.007

Chanson, H. 2006. Tsunami surges on dry coastal plains: application of dam break wave equations. *Coastal Engineering Journal*, **48**, 355–370, https://doi.org/10.1142/S0578563406001477

Dominey-Howes, D., Dunbar, P., Varner, J. and Papathoma-Köhle, M. 2010. Estimating probable maximum loss from a Cascadia tsunami. *Natural Hazards*, **53**, 43–61, https://doi.org/10.1007/s11069-009-9409-9

Farizan, A., Yaghoubi, S., Firoozabadi, B. and Afshin, H. 2019. Effect of an obstacle on the depositional behaviour of turbidity currents. *Journal of Hydraulic Research*, **57**, 75–89, https://doi.org/10.1080/00221686.2018.1459891

FEMA 2019. *Guidelines for Design of Structures for Vertical Evacuation from Tsunamis*. 3rd edn. The Applied Technology Council, https://www.weather.gov/media/itic-car/vertical_evac/FEMAP646_ThirdEdition_508.pdf

Fisher, R.V. 1983. Flow transformations in sediment gravity flows. *Geology*, **11**, 273–274, https://doi.org/10.1130/0091-7613(1983)11<273:FTISGF>2.0.CO;2

Foytong, P., Ruangrassamee, A., Shoji, G., Hiraki, Y. and Ezura, Y. 2013. Analysis of tsunami flow velocities during the March 2011 Tohoku, Japan, Tsunami. *Earthquake Spectra*, **29**, 161–181, https://doi.org/10.1193/1.4000128

Fritz, H.M., Borrero, J.C., Synolakis, C.E. and Yoo, J. 2006. 2004 Indian Ocean tsunami flow velocity measurements from survivor videos. *Geophysical Research Letters*, **33**, L24605, https://doi.org/10.1029/2006GL026784

Gibbons, S.J., Lorito, S. *et al.* 2022. The sensitivity of tsunami impact to earthquake source parameters and manning friction in high-resolution inundation simulations. *Frontiers in Earth Science*, **9**, 757618, https://doi.org/10.3389/feart.2021.757618

Goldewijk, K.K., Beusen, A., Van Drecht, G. and De Vos, M. 2011. The HYDE 3.1 spatially explicit database of human-induced global land-use change over the past 12 000 years. *Global Ecology and Biogeography*, **20**, 73–86, https://doi.org/10.1111/J.1466-8238.2010.00587.X

Goto, K., Chagué-Goff, C. *et al.* 2011. New insights of tsunami hazard from the 2011 Tohoku-oki event. *Marine Geology*, **290**, 46–50, https://doi.org/10.1016/J.MARGEO.2011.10.004

Goto, K., Hashimoto, K., Sugawara, D., Yanagisawa, H. and Abe, T. 2014. Spatial thickness variability of the 2011 Tohoku-oki tsunami deposits along the coastline of Sendai Bay. *Marine Geology*, **358**, 38–48, https://doi.org/10.1016/J.MARGEO.2013.12.015

Grezio, A., Babeyko, A. *et al.* 2017. Probabilistic tsunami hazard analysis: multiple sources and global applications. *Reviews of Geophysics*, **55**, 1158–1198, https://doi.org/10.1002/2017RG000579

Haughton, P., Davis, C., McCaffrey, W. and Barker, S. 2009. Hybrid sediment gravity flow deposits – classification, origin and significance. *Marine and Petroleum Geology*, **26**, 1900–1918, https://doi.org/10.1016/J.MARPETGEO.2009.02.012

Hayashi, S. and Koshimura, S. 2013. The 2011 Tohoku tsunami flow velocity estimation by the aerial video analysis and numerical modeling. *Journal of Disaster Research*, **8**, 561–572, https://doi.org/10.20965/jdr.2013.p0561

Hill, J., Rush, G. *et al.* 2023. Resolving tsunami wave dynamics: integrating sedimentology and numerical modelling. *The Depositional Record*, **9**, 1046–1065, https://doi.org/10.1002/DEP2.247

Hiscott, R.N. 1994. Loss of capacity, not competence, as the fundamental process governing deposition from turbidity currents. *Journal of Sedimentary Research*, **64**, 209–214, https://doi.org/10.2110/JSR.64.209

Ishimura, D. and Miyauchi, T. 2015. Historical and paleo-tsunami deposits during the last 4000 years and their correlations with historical tsunami events in Koyadori on the Sanriku Coast, northeastern Japan. *Progress in Earth and Planetary Science*, **2**, 1–18, https://doi.org/10.1186/s40645-015-0047-4

Iverson, R.M. 1997. The physics of debris flows. *Reviews of Geophysics*, **35**, 245–296, https://doi.org/10.1029/97RG00426

Jaffe, B., Goto, K., Sugawara, D., Gelfenbaum, G. and La Selle, S.P. 2016. Uncertainty in tsunami sediment transport modeling. *Journal of Disaster Research*, **11**, 647–661, https://doi.org/10.20965/JDR.2016.P0647

Jagodziński, R., Sternal, B., Szczuciński, W., Chagué-Goff, C. and Sugawara, D. 2012. Heavy minerals in the 2011 Tohoku-oki tsunami deposits – insights into sediment sources and hydrodynamics. *Sedimentary Geology*, **282**, 57–64, https://doi.org/10.1016/J.SEDGEO.2012.07.015

Julien, P.Y. 2010. Erosion and sedimentation. *In:* Julien, P.Y. (ed.) *Erosion and Sedimentation*. 2nd edn. Cambridge University Press, 216–263, https://www.cambridge.org/core/books/erosion-and-sedimentation/26384CD70C0DD5C6CCED2F55C5840411

Kaida, H., Tomita, T., Yoshimura, S. and Kihara, N. 2024. Review of evaluation of tsunami-induced debris collision force. *Coastal Engineering Journal*, **66**, 492–518, https://doi.org/10.1080/21664250.2024.2341471

Kane, I.A., Pontén, A.S.M., Vangdal, B., Eggenhuisen, J.T., Hodgson, D.M. and Spychala, Y.T. 2017. The stratigraphic record and processes of turbidity current transformation across deep-marine lobes. *Sedimentology*, **64**, 1236–1273, https://doi.org/10.1111/SED.12346

Koshimura, S., Oie, T., Yanagisawa, H. and Imamura, F. 2009. Developing fragility functions for tsunami damage estimation using numerical model and post-tsunami data from Banda Aceh, Indonesia. *Coastal Engineering Journal*, **51**, 243–273, https://doi.org/10.1142/S0578563409002004

Kunath, P., Talling, P.J., Lange, D., Chi, W.C., Baker, M.L., Urlaub, M. and Berndt, C. 2025. Ocean-bottom seismometers reveal surge dynamics in

Earth's longest-runout sediment flows. *Communications Earth & Environment 2025*, **6**, 147, https://doi.org/10.1038/s43247-025-02137-z

León, T., Lau, A.Y.A., Easton, G. and Goff, J. 2023. A comprehensive review of tsunami and palaeotsunami research in Chile. *Earth-Science Reviews*, **236**, 104273, https://doi.org/10.1016/J.EARSCIREV.2022.104273

Li, K., Salmanidou, D., Gopinathan, D., Heidarzadeh, M. and Guillas, S. 2025. Uncertainty in Manning's roughness coefficient in multilevel simulations of future tsunamis in Sumatra. *Proceedings of the Royal Society A: Mathematical, Physical and Engineering Sciences*, **481**, 757618, https://doi.org/10.1098/rspa.2024.0637

Løvholt, F., Setiadi, N.J. *et al.* 2014. Tsunami risk reduction – are we better prepared today than in 2004? *International Journal of Disaster Risk Reduction*, **10**, 127–142, https://doi.org/10.1016/J.IJDRR.2014.07.008

Lowe, D.R., Williams, S.N., Leigh, H., Connort, C.B., Gemmell, J.B. and Stoiber, R.E. 1986. Lahars initiated by the 13 November 1985 eruption of Nevado del Ruiz, Colombia. *Nature*, **324**, 51–53, https://doi.org/10.1038/324051a0

Macabuag, J., Rossetto, T., Ioannou, I. and Eames, I. 2018. Investigation of the effect of debris-induced damage for constructing tsunami fragility curves for buildings. *Geosciences*, **8**, 117–132, https://doi.org/10.3390/GEOSCIENCES8040117

MacInnes, B.T., Bourgeois, J., Pinegina, T.K. and Kravchunovskaya, E.A. 2009. Tsunami geomorphology: erosion and deposition from the 15 November 2006 Kuril Island tsunami. *Geology*, **37**, 995–998, https://doi.org/10.1130/G30172A.1

Majumdar, D. and Bhattacharya, H.N. 2025. Event beds in Andaman beach sediments – records of 2004 Tsunami. *Marine Geology*, **480**, 107470, https://doi.org/10.1016/J.MARGEO.2024.107470

Marras, S. and Mandli, K.T. 2020. Modeling and simulation of tsunami impact: a short review of recent advances and future challenges. *Geosciences*, **11**, 5–23, https://doi.org/10.3390/GEOSCIENCES11010005

Martín-Antón, M., Del Campo, J.M., Negro, V., Frades, J.L., Moreno Blasco, L.J. and Jiménez Verdejo, J.R. 2020. Land use and Port-city integration in reclamation areas: a comparison between Spain and Japan. *Journal of Coastal Research*, **95**, 278–282, https://doi.org/10.2112/SI95-054.1

Matsumoto, D., Sawai, Y. *et al.* 2023. Sedimentary diversity of the 2011 Tohoku-oki tsunami deposits on the Sendai coastal plain and the northern coast of Fukushima Prefecture, Japan. *Progress in Earth and Planetary Science*, **10**, 1–30, https://doi.org/10.1186/s40645-023-00553-3

Matsumoto, H.-A. 1985. Beach ridge ranges and the Holocene sea-level fluctuations on alluvial coastal plains, northeast Japan. *Science Reports of Tohoku University, 7th Series*, **35**, 15–46.

McCoy, S.W., Kean, J.W., Coe, J.A., Staley, D.M., Wasklewicz, T.A. and Tucker, G.E. 2010. Evolution of a natural debris flow: in situ measurements of flow dynamics, video imagery, and terrestrial laser scanning. *Geology*, **38**, 735–738, https://doi.org/10.1130/G30928.1

Minoura, K. and Nakaya, S. 1991. Traces of tsunami preserved in inter-tidal lacustrine and marsh deposits: some examples from northeast Japan. *The Journal of Geology*, **99**, 265–287, https://doi.org/10.1086/629488

Mitra, R., Naruse, H. and Abe, T. 2020. Estimation of tsunami characteristics from deposits: inverse modeling using a deep-learning neural network. *Journal of Geophysical Research: Earth Surface*, **125**, https://doi.org/10.1029/2020JF005583

Moore, A., Goff, J. *et al.* 2011. Sedimentary deposits from the 17 July 2006 western Java tsunami, Indonesia: use of grain size analyses to assess tsunami flow depth, speed, and traction carpet characteristics. *Pure and Applied Geophysics*, **168**, 1951–1961, https://doi.org/10.1007/s00024-011-0280-8

Mori, N., Takahashi, T., Yasuda, T. and Yanagisawa, H. 2011. Survey of 2011 Tohoku earthquake tsunami inundation and run-up. *Geophysical Research Letters*, **38**, L00G14, https://doi.org/10.1029/2011GL049210

Morton, R.A., Gelfenbaum, G. and Jaffe, B.E. 2007. Physical criteria for distinguishing sandy tsunami and storm deposits using modern examples. *Sedimentary Geology*, **200**, 184–207, https://doi.org/10.1016/J.SEDGEO.2007.01.003

Mulder, T. and Alexander, J. 2001. The physical character of subaqueous sedimentary density flows and their deposits. *Sedimentology*, **48**, 269–299, https://doi.org/10.1046/J.1365-3091.2001.00360.X

NCEI 2024. *NCEI/WDS Global Historical Tsunami Database*. NOAA National Centres for Environmental Information, https://doi.org/10.7289/V5PN93H7

Ngo, N. and Robertson, I.N. 2012. *Video Analysis of the March 2011 Tsunami in Japan's Coastal Cities*. University of Hawaii Research Report **UHM/CEE/12-11**, 1–94.

NHK World 2011. NHK World Video coverage – CNN – YouTube. CNN, https://www.youtube.com/watch?v=zxm050h0k2I&t=3s

NHK World 2021. 3/11 – the Tsunami: the first 3 days – documentary, https://www3.nhk.or.jp/nhkworld/en/ondemand/video/3016087/

Nistor, I., Goseberg, N. and Stolle, J. 2017. Tsunami-driven debris motion and loads: a critical review. *Frontiers in Built Environment*, **3**, 245673, https://doi.org/10.3389/fbuil.2017.00002

Noda, A., Kondoh, A. and Nishihiro, J. 2019. Changes in land cover and grassland area over the past 120 years in a rapidly urbanised area in Japan. *One Ecosystem*, **4**, e37669, https://doi.org/10.3897/ONEECO.4.E37669

Ortleb, S., Lambrechts, J. and Kärnä, T. 2022. Wetting and drying procedures for shallow water simulations. *In:* Schuttelaars, H., Heemink, A., Deleersnijder, E. (eds) *The Mathematics of Marine Modelling. Mathematics of Planet Earth*. Springer, 287–314, https://doi.org/10.1007/978-3-031-09559-7_11

Ozawa, A., Mimura, K. and Kubo, K. 1987. *Geological Map of Sendai (1:200 000 Geological Map Width)*. Geological Survey of Japan.

Peakall, J., Best, J. *et al.* 2020. An integrated process-based model of flutes and tool marks in deep-water environments: implications for palaeohydraulics, the Bouma sequence and hybrid event beds. *Sedimentology*, **67**, 1601–1666, https://doi.org/10.1111/sed.12727

Pierson, T.C. 2005. Hyperconcentrated flow – transitional process between water flow and debris flow. *In:* Jakob, M. and Hungr, O. (eds) *Debris-Flow Hazards and Related Phenomena*. *Springer Praxis Books*. Springer, Berlin, 159–202, https://doi.org/10.1007/3-540-27129-5_8

Pilarczyk, J.E., Horton, B.P., Witter, R.C., Vane, C.H., Chagué-Goff, C. and Goff, J. 2012. Sedimentary and foraminiferal evidence of the 2011 Tōhoku-oki tsunami on the Sendai coastal plain, Japan. *Sedimentary Geology*, **282**, 78–89, https://doi.org/10.1016/J.SEDGEO.2012.08.011

Pollard, O.G., Barlow, N.L.M., Gregoire, L.J. and Gomez, N. 2024. Relative sea-level sensitivity in the Eurasian region to Earth and ice-sheet model uncertainty during the Last Interglacial. *Quaternary Science Reviews*, **343**, 108908, https://doi.org/10.1016/J.QUASCIREV.2024.108908

Richmond, B., Szczuciński, W. *et al.* 2012. Erosion, deposition and landscape change on the Sendai coastal plain, Japan, resulting from the March 11, 2011 Tohoku-oki tsunami. *Sedimentary Geology*, **282**, 27–39, https://doi.org/10.1016/J.SEDGEO.2012.08.005

Röbke, B.R. and Vött, A. 2017. The tsunami phenomenon. *Progress in Oceanography*, **159**, 296–322, https://doi.org/10.1016/J.POCEAN.2017.09.003

Sato, S., Okayasu, A., Yeh, H., Fritz, H.M., Tajima, Y. and Shimozono, T. 2014. Delayed survey of the 2011 Tohoku tsunami in the former exclusion zone in Minami-Soma, Fukushima Prefecture. *Pure and Applied Geophysics*, **171**, 3229–3240, https://doi.org/10.1007/s00024-014-0809-8

Sawai, Y., Namegaya, Y., Okamura, Y., Satake, K. and Shishikura, M. 2012. Challenges of anticipating the 2011 Tohoku earthquake and tsunami using coastal geology. *Geophysical Research Letters*, **39**, L21309, https://doi.org/10.1029/2012GL053692

Schöffl, T., Nagl, G., Koschuch, R., Schreiber, H., Hübl, J. and Kaitna, R. 2023. A perspective of surge dynamics in natural debris flows through pulse-Doppler radar observations. *Journal of Geophysical Research: Earth Surface*, **128**, e2023JF007171, https://doi.org/10.1029/2023JF007171

Sharrocks, P.D., Peakall, J., Hodgson, D.M. and Barlow, N.L.M. 2025. Tsunami versus storms: diagnostic sedimentary criteria in coastal lakes, lagoons and sinkhole deposits. *Earth-Science Reviews*, **271**, 105277, https://doi.org/10.1016/J.EARSCIREV.2025.105277

Shen, X., Lin, M., *et al.* 2024. Viscosity of cohesive sediment-laden flows: experimental and empirical methods. *Journal of Geophysical Research: Oceans*, **129**, e2023JC020043, https://doi.org/10.1029/2023JC020043

Shige-eda, M. and Akiyama, J. 2003. Numerical and experimental study on two-dimensional flood flows with and without structures. *Journal of Hydraulic Engineering*, **129**, 817–821, https://doi.org/10.1061/(ASCE)0733-9429(2003)129:10(817)

Sihombing, Y.I., Adityawan, M.B. *et al.* 2019. Tsunami overland flow characteristic and its effect on Palu Bay due to the Palu tsunami 2018. *Journal of Earthquake and Tsunami*, **14**, 1–22, https://doi.org/10.1142/S1793431120500098

Simons, M., Minson, S.E. *et al.* 2011. The 2011 magnitude 9.0 Tohoku-Oki earthquake: mosaicking the megathrust from seconds to centuries. *Science*, **332**, 1421–1425, https://doi.org/10.1126/SCIENCE.1206731

Strusińska-Correia, A. 2017. Tsunami mitigation in Japan after the 2011 Tōhoku Tsunami. *International Journal of Disaster Risk Reduction*, **22**, 397–411, https://doi.org/10.1016/J.IJDRR.2017.02.001

Sugawara, D. 2021. Numerical modeling of tsunami: advances and future challenges after the 2011 Tohoku earthquake and tsunami. *Earth Science Reviews*, **214**, 103498, https://doi.org/10.1016/J.EARSCIREV.2020.103498

Sugawara, D., Goto, K. and Jaffe, B.E. 2014. Numerical models of tsunami sediment transport – current understanding and future directions. *Marine Geology*, **352**, 295–320, https://doi.org/10.1016/J.MARGEO.2014.02.007

Suppasri, A., Charvet, I., Imai, K. and Imamura, F. 2015. Fragility curves based on data from the 2011 Tohoku-Oki tsunami in Ishinomaki City, with discussion of parameters influencing building damage. *Earthquake Spectra*, **31**, 841–868, https://doi.org/10.1193/053013EQS138M

Syamsidik, S., Luthfi, M., Fauzi, A. and Fatimah, E. 2019. Numerical experiments on tsunami wave forces on open structures using dam-break method. *IOP Conference Series: Earth and Environmental Science*, **273**, 012010, https://doi.org/10.1088/1755-1315/273/1/012010

Synolakis, C.E. and Kong, L. 2006. Runup measurements of the December 2004 Indian Ocean tsunami. *Earthquake Spectra*, **22**, 67–91, https://doi.org/10.1193/1.2218371

Szczuciński, W., Kokociński, M., Rzeszewski, M., Chagué-Goff, C., Cachão, M., Goto, K. and Sugawara, D. 2012. Sediment sources and sedimentation processes of 2011 Tohoku-oki tsunami deposits on the Sendai Plain, Japan – insights from diatoms, nannoliths and grain size distribution. *Sedimentary Geology*, **282**, 40–56, https://doi.org/10.1016/J.SEDGEO.2012.07.019

Takashimizu, Y., Urabe, A., Suzuki, K. and Sato, Y. 2012. Deposition by the 2011 Tohoku-oki tsunami on coastal lowland controlled by beach ridges near Sendai, Japan. *Sedimentary Geology*, **282**, 124–141, https://doi.org/10.1016/J.SEDGEO.2012.07.004

Talling, P.J., Masson, D.G., Sumner, E.J. and Malgesini, G. 2012. Subaqueous sediment density flows: depositional processes and deposit types.

*Sedimentology*, **59**, 1937–2003, https://doi.org/10.1111/J.1365-3091.2012.01353.X

Tappin, D.R., Evans, H.M., Jordan, C.J., Richmond, B., Sugawara, D. and Goto, K. 2012. Coastal changes in the Sendai area from the impact of the 2011 Tōhoku-oki tsunami: interpretations of time series satellite images, helicopter-borne video footage and field observations. *Sedimentary Geology*, **282**, 151–174, https://doi.org/10.1016/J.SEDGEO.2012.09.011

Thouret, J.C., Antoine, S., Magill, C. and Ollier, C. 2020. Lahars and debris flows: characteristics and impacts. *Earth-Science Reviews*, **201**, 103003, https://doi.org/10.1016/J.EARSCIREV.2019.103003

Vallance, J.W. and Iverson, R.M. 2015. Lahars and their deposits. *In:* Sigurdsson, H. (ed.) *The Encyclopedia of Volcanoes*. Academic Press, 649–664, https://doi.org/10.1016/B978-0-12-385938-9.00037-7

Verykokou, S. and Ioannidis, C. 2024. Oblique aerial images: geometric principles, relationships and definitions. *Encyclopedia*, **4**, 234–255, https://doi.org/10.3390/ENCYCLOPEDIA4010019

von Häfen, H., Krautwald, C., Bihs, H. and Goseberg, N. 2022. Dam-Break waves' hydrodynamics on composite bathymetry. *Frontiers in Built Environment*, **8**, 877378, https://doi.org/10.3389/fbuil.2022.877378

Wang, J., Zhang, K., Li, P., Meng, Y. and Zhao, L. 2021. Hydrodynamic characteristics and evolution law of roll waves in overland flow. *CATENA*, **198**, 105068, https://doi.org/10.1016/J.CATENA.2020.105068

Warner, J.C., Sherwood, C.R. *et al.* 2025. Numerical simulation of sound-side barrier-island inundation and breaching during Hurricane Dorian (2019). *Journal of Geophysical Research: Earth Surface*, **130**, e2025JF008309, https://doi.org/10.1029/2025JF008309

Yamashita, K., Sugawara, D., Goto, K., Ishizawa, T. and Takahashi, T. 2025. A similarity law for sandy tsunami deposits. *Journal of Geophysical Research: Earth Surface*, **130**, e2024JF008244, https://doi.org/10.1029/2024JF008244

Yoshii, T., Tanaka, S. and Matsuyama, M. 2017. Tsunami deposits in a super-large wave flume. *Marine Geology*, **391**, 98–107, https://doi.org/10.1016/J.MARGEO.2017.07.020

Yoshii, T., Tanaka, S. and Matsuyama, M. 2018. Tsunami inundation, sediment transport, and deposition process of tsunami deposits on coastal lowland inferred from the Tsunami Sand Transport Laboratory Experiment (TSTLE). *Marine Geology*, **400**, 107–118, https://doi.org/10.1016/J.MARGEO.2018.03.007

Zanuttigh, B. and Lamberti, A. 2007. Instability and surge development in debris flows. *Reviews of Geophysics*, **45**, RG3006, https://doi.org/10.1029/2005RG000175

Zarch, M.K., Zhang, L.M., Haeri, S.M. and Xu, Z.D. 2022. Rheological behaviour of dilute soil-water mixtures: role of interactions from colloidal and non-colloidal particles. *Canadian Geotechnical Journal*, **60**, 139–150, https://doi.org/10.1139/cgj-2021-0437